Enhanced piezoelectric performance of multi-layered flexible polyvinylidene fluoride–BaTiO$_3$–rGO films for monitoring human body motions

Yinhui Li[1], Jianqiang Tan[1], Kun Liang[1], Yong Li[1], Jiaojiao Sun[1], Hulin Zhang[1], Cuixian Luo[2], Pengwei Li[1,*] (ID), Jianle Xu[1,*], Huabei Jiang[3], and Kaiying Wang[4]

[1] *Micro-Nano System Research Center, College of Information and Computer, Taiyuan University of Technology, Taiyuan 030024, Shanxi, China*

[2] *Information College, Shanxi University of Finance and Economics, Taiyuan 030006, China*

[3] *Department of Medical Engineering, College of Engineering, University of South Florida, Tampa, FL 33620, USA*

[4] *Department of Microsystems, University of South-Eastern Norway, 3184 Horten, Norway*

ABSTRACT

Poly(vinylidene fluoride) (PVDF)/Barium titanate (BaTiO$_3$, BTO)/reduced graphene oxide (rGO) (BTO/PVDF/rGO) ternary flexible piezoelectric composite films were successfully prepared, and multi-layered PVDF/BTO/rGO composite piezoelectric nanogenerator (PNG) was also designed via layer-by-layer method. The maximum output value of the PVDF/BTO/rGO PNG achieves at 4-layered design when the rGO content is 0.5 wt%. The output voltage and current are 16.91 V, 3.53 μA, which is 18.9% and 45.9% higher than 4-layered PNGs without rGO, respectively. In addition, the relative dielectric constant was increased by 72.67% and the Pr was increased by 27.47% compared with the composite film without rGO. Finally, the feasibility of the practical application was verified by using composite PNG to charge the capacitor, and over 4000 cycles pressing-releasing test demonstrated its mechanical reliability and stability. Simple-structured and self-charged PNGs were performed onto a finger, wrist, elbow joints, and sole of foot, which suggested PNGs were successfully applied as potential platforms for distinctively monitoring a wide range of human body motions in real time. These promising features of PVDF/BTO/rGO flexible PNGs will promote potential applications in the fields of human movement monitoring, intelligent skin, and soft robotics.

Address correspondence to E-mail: lipengwei@tyut.edu.cn; xujianle@tyut.edu.cn

Springer

1 Introduction

Recently, flexible piezoelectric sensors have attracted considerable attention due to their high output constant and self-powered property for widely use in nanoelectronics, including memory devices, transistors, capacitors, nanogenerators, etc. [1–3]. Over the past decades, considerable efforts have been made to develop flexible piezoelectric materials that possesses a high dielectric constant and output performance. Combining polymer with piezoelectric ceramic has been proven to be an effective method to prepare flexible composite piezoelectric materials [4, 5]. Several inorganic piezoelectric ceramic materials including $PbZr_{1-x}Ti_xO_3$ (PZT) [6], $PbTiO_3$ (PT) [7], $Pb(Mg_{1/3}Nb_{2/3})O_3$ (PMN) [8], and $BaTiO_3$ (BTO) [9], etc. have been selected to form piezoelectric nanogenerator (PNG). Although they reveal high piezoelectric coefficients for energy conversion, but they are cost intensive, toxic, brittle in nature. Thus, environmentally stable, biocompatible, and flexible PVDF nanocomposites that easy preparative methods with cost effectiveness are one of the better alternative ways to overcome pure inorganic piezoelectric device limitations [10].

Various approaches have been employed to improve the energy harvesting performance of piezoelectric ceramic composite based on polymer materials. Recently, several research groups have attempted to improve piezoelectric properties of the composite films by combination of PVDF with doping carbonaceous materials, such as carbon nanotubes (CNTs) [11, 12], graphene [13–15], and carbon black [4]. The reasons for piezoelectric properties enhancement can be summarized as follows: (i) the carbon-containing compound can make nanoparticles (e.g., BTO) more uniformly dispersed in the polymer; (ii) the formation of conductive path can reduce the internal resistance of the PNG and reduce the current loss during the charging and discharging process, thereby improving the output performance.

Graphene, a classical two-dimensional material, has received great attention due to its distinctive electrical and mechanical properties [16–20]. Recently, graphene demonstrates to be a promising filler material for flexible PNGs, in which the piezoelectric behavior results from the instant contact of isolated graphene sheets or islands. On the one hand, the employment of graphene as a conductive filler in

polymer ceramic, e.g., PVDF–BTO nanocomposites, will effectively enhance the dielectric and ferroelectric properties. A few research results have been published on PVDF–BTO and graphene composite-based flexible piezoelectric materials. Usman Yaqoob et al. reported piezoelectric nanocomposites based on PVDF–rGO–BTO showed dielectric constant 98, a very low leakage Current density (1.29×10^{-7} A/cm^2) [21]. On the other hand, graphene oxide nanosheets can also act as nucleating agent to promote PVDF piezoelectric phase transition [22]. Owing to the strong and specific interaction between the carbonyl groups (C=O) on the surface of rGO and the fluorine group (=CF_2) of PVDF, incorporating a carbonyl group (C=O) containing filler such as rGO into PVDF matrix results in their uniform dispersion/distribution [23, 24]. This in turn results in the formation of a β-polymorph structure as well as enhancements of the electrical and mechanical properties of PVDF-based composite materials. Additionally, multi-layered structure design can enhance the output performance that obviously has been proved in our previous work [25]. However, low output voltage and current limit the practical application of PNGs, and it is urgent to found a solution to further improve output performance of multi-layered PNGs. A certain amount of rGO addition has been proved to be an efficient method to enhance output properties of PNGs [26–29], while multi-layered rGO composite PNGs have not been designed and if it can improve the performance of multi-layered composite, PNGs are still unclear.

Hence, PVDF/BTO/rGO ternary flexible composite films were successfully prepared, and in this part, rGO was employed as a conductive filler in PVDF/BTO and the effects of rGO addition on phase transformation of PVDF and output performance have been systematical investigated. Optimizing the rGO concentration in the PVDF/BTO matrix was explored. Moreover, multi-layered PVDF/BTO/rGO flexible composite PNGs were designed. Output performance, dielectric, piezoelectric, and ferroelectric properties of composite films were comprehensively studied, which provided a theoretical basis of the application of PVDF/BTO/rGO composite film. Finally, 4-layered structure PVDF/BTO/rGO composite was selected to pack simple device to monitor human joints movement in real time. Also, the composite PNGs can be used to develop flexible piezoelectric energy harvesting devices or sensors like

piezoelectric shoes, walkways, etc. that use vertical compression as the input.

2 Experimental section

2.1 Materials

Barium acetate [Ba(CH₃COO)₂, 99.0%], tetrabutyl titanate [$C_{16}H_{36}O_4Ti$, 98.0%], potassium hydroxide (KOH, 99.0%), poly(vinylidene fluoride) (PVDF, Weight-average molecular weight (M_w) = 4.0×10^5, 99.5%), N-N dimethylformamide (DMF, 99.0%), ethanol (C_2H_6O, 95.0%), acetone (CH_3COCH_3, 99.5%), and all the reagents were purchased from Sinopharm Chemical Reagent Co. Ltd., and used without further purification. Reduced graphene oxide (rGO) was procured from Nanjing Jicang Nano Technology Co., Ltd.

2.2 Fabrication of the PVDF/BTO/rGO nanogenerator

2.2.1 Preparation of PVDF/BTO/rGO composite film

To prepare PVDF/BTO/rGO composite films, 0.15, 0.25, 0.35, and 0.45 wt% of rGO powders were dispersed in DMF by ultrasonication for 3 h, and then 20 wt% BTO nanoparticles (BTO NPs) were added to rGO/DMF dispersion and stirring for 2 h. After that 15 wt% PVDF powder was slowly added into BTO/rGO/DMF mixture solution and then ultrasonicated for 2 h and stirring for another 30 min to obtain a homogeneous PVDF/BTO/rGO composite spincoating solution. The PVDF/BTO/rGO suspension was dropped on a dried and cleaned ITO glass substrate by spin coating, and then the samples were placed on a hot plate at 90 °C for 10 min. In order to avoid wrinkling and curling, the composite films were cured and peeled off quickly. The composite films were poled at 100 °C by applying 15 KV/m electric field for 3 h. BTO/PVDF composite films were synthesized in the same manner but without addition of rGO.

2.2.2 Fabrication of PNGs

Two copper electrodes were taped on the synthesized BTO/PVDF and PVDF/BTO/rGO composite films (2.5 cm × 2.5 cm), and then two copper wires were welded on the both sides of copper electrodes. Multilayered BTO/PVDF and PVDF/BTO/rGO composite films (2.5 cm × 2.5 cm) with the same thickness (~ 15 μm) were assembled vertically layer by layer. The same copper electrodes manufacture process was conducted onto top and bottom sides of multi-layered composite films. Thin poly(ethylene terephthalate) (PET, 300 μm) was pasted onto both side of copper electrons to enhance robustness of the device and protect the device from external mechanical stress, temperature, and humidity. Schematic diagram for PVDF/BTO/rGO composite film PNG fabrication is shown in Scheme 1.

2.3 Characterization

The morphologies of the as-prepared BTO NPs, BTO/rGO, and the surface of PVDF/BTO/rGO composite film were characterized using field emission scanning electron microscope (FESEM, model JEOL JSM-7001, Japan). All SEM samples were sputter coated with gold particles before observation. The particle size and size distributions were estimated based on the measured values. The crystal structure of prepared samples was measured by X-ray diffraction (XRD, Rigaku Co., Tokyo, Japan) with Cu Kα₁ (λ = 0.154056 Å) radiation. The XRD measurements were performed in a 2θ range from 10° to 80° with scanning speed of 2°/min. The microstructure of BTO/rGO composite was observed by transmission electron microscopy (TEM, JEOL, 2100 F, Japan) at an acceleration voltage of 200 KV. IR spectra ranged from 400 to 1000 cm⁻¹ number wave were obtained by a FTIR instrument (Bruker, model IFS 48) with resolutions of the order of 1 cm⁻¹. The Raman spectra were recorded using a Holoprobe Kaiser optical spectrometer (VV mode, Renishaw, UK) with a spot size of about 1 μm. A 532 nm laser excitation source with a 5-s integration time per spectrum was focused on the composite films via a 50 × objective lens. Relative permittivity and dielectric loss were measured by ferroelectric testing system (RTI-Multiferroic, Radiant Technologies, USA) at room temperature with a frequency range from 10³ to 10⁶ Hz at 1 V_rms. The polarization–electric hysteresis loop (P–E) was measured by ferroelectric analyzer (RTI-Multiferroic of Radiant, USA) with the frequency of 1 Hz at room temperature. The open-circuit output voltage of composite PNGs under repeated beating were

Scheme 1 Schematic diagram of the BTO/rGO/PVDF composite film PNG
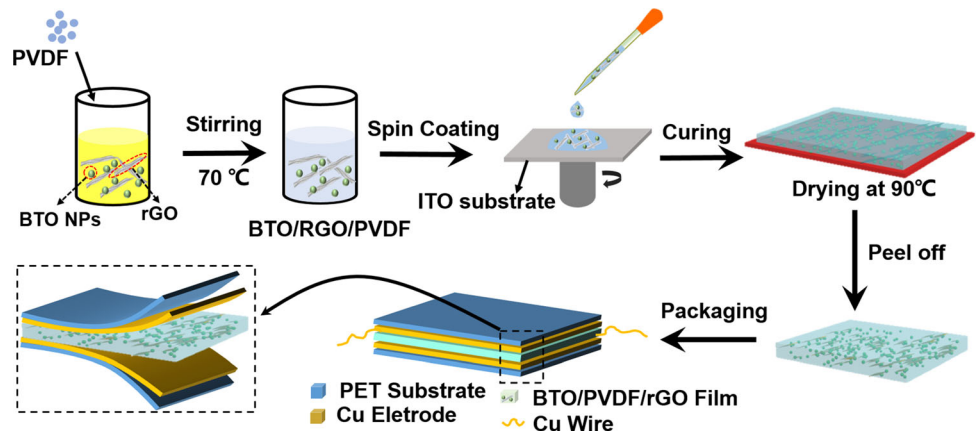
measured by a test system platform which has been built in our previous work [9]. The short-circuit current of the PVDF/BTO/rGO composite PNGs was recorded by a source measurement unit (2400 SMU, Keithley, USA).

3 Results and discussion

3.1 Morphology and structure

The morphological structure of the synthesized BTO NPs, BTO/rGO, and PVDF/BTO/rGO composite film was characterized by SEM and TEM. Figure 1a and b shows FESEM image of BTO NPs and its diameter distribution, respectively. It can be clearly seen that the BTO NPs present sphere-like nanostructure, and the average size of individual BTO nanospheres is $\sim 65 \pm 20$ nm. The XRD pattern in Fig. S1 illustrates that BTO NPs are a typical tetragonal crystal phase structure. Figure 1c shows that the BTO nanoparticles are mostly uniformly distributed in the composite film, and there is still a small amount of agglomeration because of the relative high viscosity of PVDF/BTO/rGO spin-coating solution. Figure 1d displays the TEM images of BTO/rGO

Fig. 1 **a** SEM image of BTO NPs; **b** the corresponding diameter histogram of BTO NPs is shown in (**a**); **c** Surface SEM image of PVDF/BTO/rGO composite film; **d** TEM image of BTO/rGO composite material; **e** HRTEM image of BTO NPs labeled by white rectangle in (**d**)
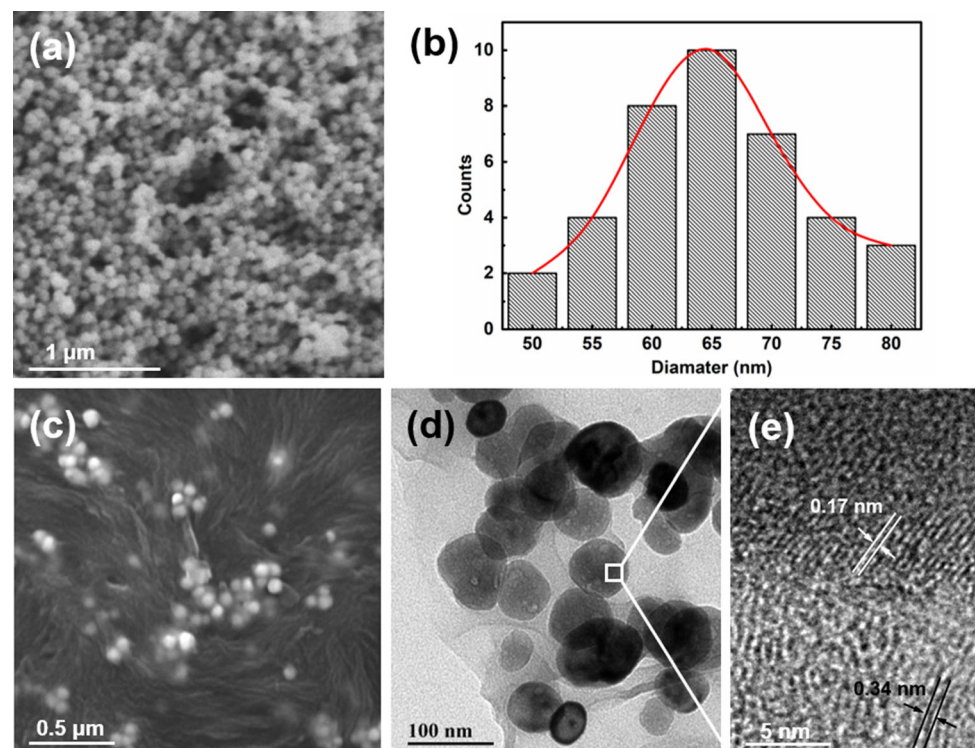
composite, and the BTO NPs are good spherical microstructure and well dispersed isolated into the GO matrix. The HRTEM image obtained from the white rectangles in Fig. 1d shows a perfectly resolved lattice spacing of 0.17 nm with BTO, corresponding to hematite (011) lattice facet, and with GO lattice spacing of 0.34 nm, corresponding to carbon (100) lattice facet.

In order to investigate the effect of rGO doping on the composite film, the XRD patterns of the pure PVDF film, PVDF/BTO, and PVDF/BTO/rGO composite film with different rGO contents of 0.15, 0.25, 0.35, and 0.45 wt% are shown in Fig. 2. As shown in Fig. 2, a large diffraction peak at around 20.3° could be observed in pure PVDF film, referring to the polar β-phase of PVDF caused by the diffraction of (110) and (200) facets [30]. The diffraction patterns demonstrate ten distinct peaks centered at $2\theta = 22.1°$, 31.6°, 38.8°, 45.2°, 50.8°, 56.1°, 65.8°, 70.3°, 74.7°, and 79.0° corresponding to (100), (110), (111), (200), (210), (211), (320), (300), (310), and (311) crystal planes of tetragonal BTO NPs, which coincides with typical diffraction peaks of pure BTO NPs (Fig. S1). The intensity of typical peak characterized by rGO at $2\theta = 25.4°$ becomes stronger and stronger with the rGO content increasing. Moreover, the β-peak of PVDF ($2\theta = 20.3°$) intensity increases first and then decreases with increase in rGO content. This phenomenon could be explained with the interaction
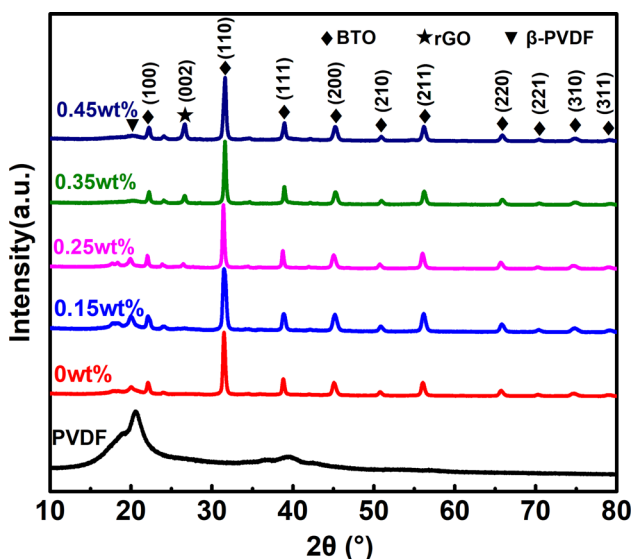

Fig. 2 XRD patterns of PVDF film, BTO/PVDF, and BTO/PVDF/rGO composite films with different contents of rGO

between PVDF and rGO. The rGO content increases from 0 to 1.5 to 2.5 wt%, and molecular chains of PVDF are induced by rGO. The –CH$_2$ dipole of rGO and –CF$_2$ dipole of PVDF orientate together to build up a composed structure [31]; thus, β-peak intensity enhanced. The β-peak intensity decreases when the rGO amount reaches 0.35 and 0.45 wt%. That may be because the addition of excessive rGO leads to agglomeration and restricts the conformational transition of PVDF.

Fourier transform infra-red (FTIR) spectroscopy has been used for analyzing the phase formation of nanocomposite PVDF/BTO films with rGO weight percentages of 0, 0.15, 0.25, 0.35, and 0.45 wt% (weight to total mass). The results are shown in Fig. 3a. In each sample, the appearance of absorption bands at 470 and 840 cm^{-1} is assigned to the formation of β-phase for PVDF, and absorption bands at 531, 612, and 764 cm^{-1} are evidence of a certain amount of α-phase existence. To identified the relative amount of β-phase $F(\beta)$ present in the composite film samples, $F(\beta)$ is calculated by using the Beer-Lambert theory Eq. (1) [32]:

$$F(\beta) = \frac{X_\beta}{X_a + X_\beta} \times 100\%$$
$$= \frac{A_\beta}{(k_\beta/k_a)\, A_a + A_\beta} \times 100\%, \tag{1}$$

where A_α and A_β represent the absorption intensity of the typical phase and -phase (at 531 and 840 cm^{-1}), respectively. X_α and X_β are the corresponding crystallinities of the α-phase and β-phase; k_α and k_β are corresponding absorption coefficients with the values 6.1×104 cm^2/mol and 7.7×104 cm^2/mol, respectively.

The relative amount of $F(\beta)$ for the PVDF composite films has been calculated by Eq. (1), and the results are shown in Table 1. The $F(\beta)$ of PVDF/BTO/rGO composite films increased from 46.5 to 49.4 to 62.5% with the rGO content increase from 0 to 0.15 to 0.25 wt%, which indicated that the addition of rGO can induce β-phase of PVDF formation. That may be because rGO serves as nucleation points to facilitate the formation of the polar β phase in PVDF [33]. Besides, the intensive interaction between large π bond of rGO and the fluorine atom in the PVDF macromolecular chains may play an important role in the formation of β phase. However, the $F(\beta)$ of PVDF/BTO/rGO composite films decreases from

Fig. 3 a FTIR spectra and **b** Raman spectra of pure PVDF/BTO and PVDF/BTO/rGO nanocomposite films at different rGO loadings
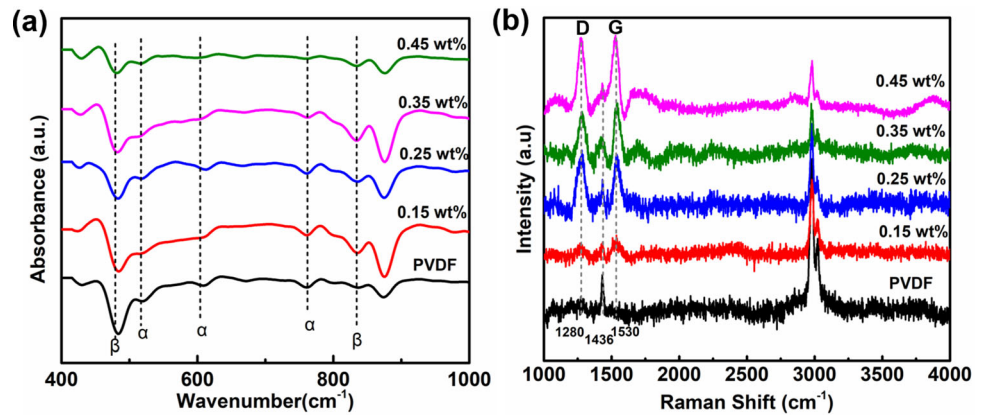

Table 1 Summary of $F(\beta)$ and I_D/I_G values of PVDF/BTO/rGO composite film with different rGO contents

rGO content	0 wt%	0.15 wt%	0.25 wt%	0.35 wt%	0.45 wt%
$F(\beta)$ (%)	46.5	49.4	62.5	59.2	57.2
I_D/I_G	/	0.85	0.87	0.88	0.90

59.2 to 57.2% when the addition of rGO content increases from 0.35 to 0.45 wt%. PVDF macromolecular chains motion is limited by agglomerate of excessive graphene, which is not benefit for inducing the formation of β phase in PVDF. Those results indicated that the addition of rGO has a significant influence on BTO/PVDF composite films, especially the transition of β phase in PVDF.

Raman spectroscopy of PVDF/BTO/rGO composite films is displayed in Fig. 3b. From Fig. 3b, the well-defined D and G bands of rGO were appeared at 1280 and 1597 cm^{-1}, respectively. In PVDF/BTO composite without rGO sample, peak corresponding to the D and G band was not observed and an obvious peak at 1436 cm^{-1} appeared due to C_α–C_β scissoring vibrations of pure PVDF [34]. In comparison, peaks of the D and G bands for the composite films with rGO contents 0.15, 0.25, 0.35, and 0.45 wt% exhibited gradually strong and broad. The I_D/I_G ratio of composite films was calculated and the results are displayed in Table 1. A slight increment was observed in I_D/I_G values with the rGO content increasing, which indicated defects in the graphene structure slightly increase.

3.2 Electrical characterization of single layered composite film

In order to investigate the influence of rGO concentration on the output capability of the PNG, a series

of PNGs were fabricated on the basis of the PVDF/BTO/rGO composite with various mass fractions rGO (0, 0.15, 0.25, 0.35, and 0.45 wt%), and BTO content selected 30 wt% according to our previous study [25]. The open-circuit voltage and short-circuit current under the same mechanical force ($F = 0.2$ MPa) and with the same film thickness (THK = 60 μm) are shown in Fig. 4. The color of the PVDF/BTO/rGO piezoelectric composite films with different rGO increasing gradually darkens from inset images in Fig. 4b. As observed from Fig. 4, when the rGO filler loading content increases from 0 to 0.15 to 0.25 wt%, the output voltage increases from 2.37 to 3.49 to 4.65 V and the short-circuit current increases from 0.34 to 0.53 to 1.82, respectively. This result can be explained by (i) percolation theory: the carbon materials (such as acetylene black, CNTs, rGO, and C_{60}) were usually employed as conductive phase in piezoelectric composite to improve the migration rate of the polarization charges; when the rGO content is below the threshold (rGO = 0.25 wt%), there is synergy between the conductive property and piezoelectric property, the finally result in the increase of the output performance; (ii) formation of micro-capacitor [35], lots of free charges are distributed on the surface of rGO nanosheets because of its high fluidity, and these free charges are accumulated by the dipoles of PVDF and BTO nanoparticles and, thus, generate new dipoles at this specific location. However, when the rGO content further increases from 0.35 to 0.45, the output voltage and short-circuit

Fig. 4 Output voltage and current of PVDF/BTO/rGO composite film with 0, 0.15, 0.25, 0.35, and 0.45 wt% rGO content
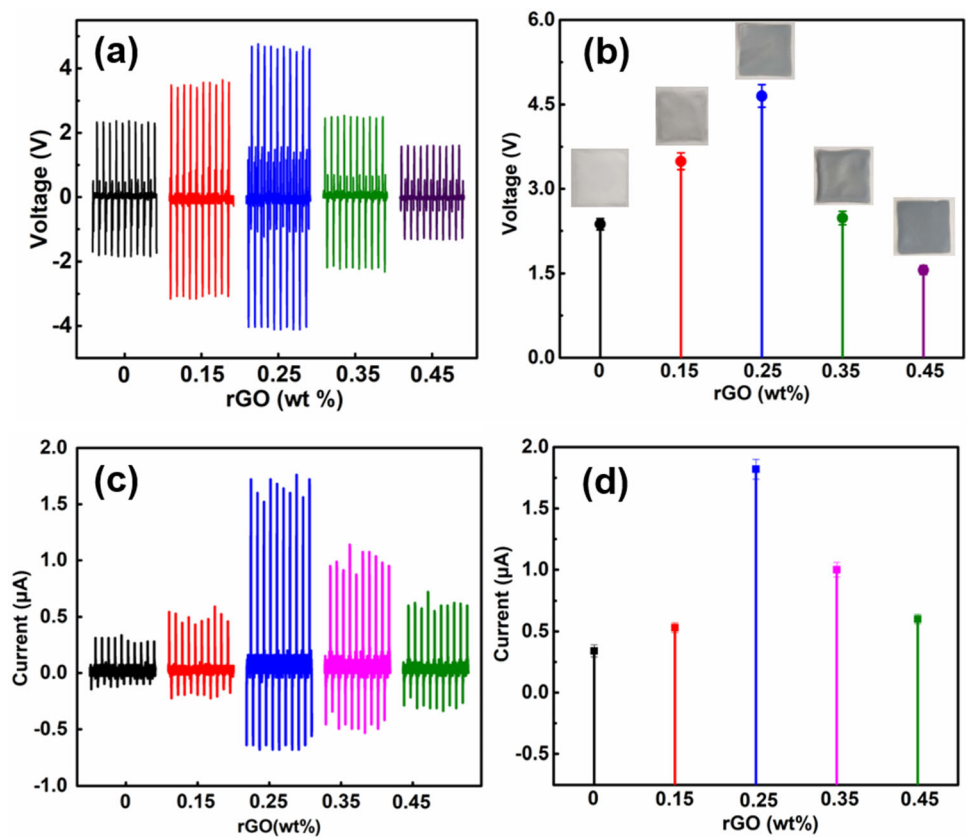
current decrease from 2.48 to 1.56 V and from 1.02 to 0.61 µA, respectively. The decrement of the voltage and current of BTO/PVDF/rGO composite film is owing to agglomeration and percolation effect of the nanofiller rGO in the polymer composite [36, 37]. With the increase of rGO content, there will be a large amount of extra free charges of rGO that cannot find the corresponding dipoles in PVDF and BTO nanoparticles. Therefore, those free charges inside the composite material make the composite material that gradually becomes a conductor. That will have a negative effect on the performance of the PNG, and results in decrease of output voltage and current.

To further explain the effect of the rGO on output performance of the PVDF/BTO/rGO composite PNGs, the relative permittivity (ε_r) at frequency range from 10^3 to 10^6 Hz and residual polarization (P_r) of composite film with different rGO contents (0, 0.15, 0.25, 0.35, and 0.45 wt%) have been characterized and the results are shown in Fig. 5. From Fig. 5a, it was found that dielectric constants of the composite films decrease as the testing frequency increases. This phenomenon could be ascribed to the interfacial

polarizations at the conductor–insulator interface occurring in composite samples due to the decrease in relaxor polarization [38, 39]. Additionally, the ε_r value in Table 2 is measured at 10^3 Hz and the ε_r varies with the rGO content. The ε_r increases from 17.96 to 21.31 to 29.19 when the content rGO increase from 0 to 0.15 to 0.25 wt%. However, as the rGO further increases from 0.35 to 0.45 wt%, ε_r decreases from 19.63 to 12.58. The increase of ε_r after introducing rGO can be attributed to the formation of many micro-capacitors inside the PVDF/BTO/rGO composite matrix, and this effect will be weakened by agglomeration of excessive rGO addition. Polarization properties of composite PNGs are found to obey similar rule. As shown in P–E loops of composite samples, the P_r of PVDF/BTO/rGO composite film increases from 0.39 to 0.46 to 0.56 µC/cm^2 when the rGO content increases from 0 to 0.15 to 0.25 wt%. while P_r value decreases from 0.29 to 0.19 µC/cm^2 as the rGO content further increases from 0.35 to 0.45 wt%. The J–E curves are shown in Fig. S3, and the leakage current density was first decreased and then increased with the increasing rGO content. In general, ferroelectricity of the composite film will be

Fig. 5 **a** The relative permittivity; **b** P–E loop characterizations of PVDF/BTO/rGO composite thin films with 0, 0.15, 0.25, 0.35, and 0.45 wt% rGO content
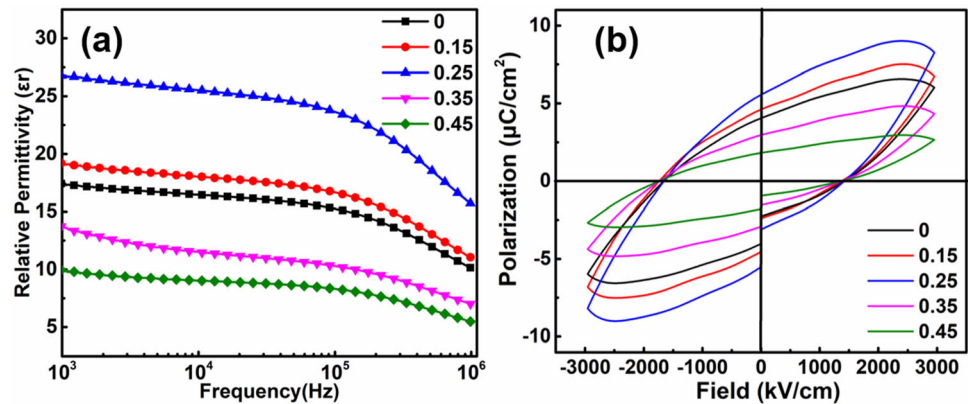

Table 2 Summary of the electrical data for the PVDF/BTO/rGO composite film with different rGO contents

rGO (wt%)	Voltage (V)	Current (µA)	ε_r (10^3 Hz)	P_r (µC/cm^2)	d_{33} (pc/N)
0	2.37	0.34	17.96	0.39	11.90
0.15	3.49	0.53	21.31	0.46	17.35
0.25	4.65	1.82	29.19	0.56	32.69
0.35	2.48	1.00	19.63	0.29	28.93
0.45	1.56	0.61	12.58	0.19	4.23

*Q_{11} in Eq. (2) was selected as 0.1 m^4/C^2

affected by microstructure of the composite film, and doping of rGO changes the domain structure of the composite film [40]. When the rGO content increases to 0.25 wt%, the domain structure of the composite film is not suppressed due to the suppression of its oxygen vacancies, which ultimately enhances the P_r value [41]. When the composite film contains an excessive amount of rGO, the formation of oxygen vacancies in the composite film is enhanced and P_r value decreases [42]. It is known that piezoelectric coefficient d_{33} determined the performance of piezoelectric materials, which is closely related to their ε_r and P_r values and d_{33} can be calculated by Eq. (2) [8, 43]:

$$d_{33} = 2Q_{11}e_0e_rP_r, \tag{2}$$

where ε_0 is the permittivity of vacuum ($\varepsilon_0 = 8.854 \times 10^{-12}$ F/m), and Q_{11} (0.05–0.1 m^4/C^2) is the electrostrictive constant of the paraelectric phase. According to Eq. (2), the d_{33} of PVDF/BTO/rGO composite PNGs could be simply calculated and the results are shown in Table 2. The d_{33} increases first (the content of rGO increases from 0 to 0.15 to 0.25 wt%) and then decreases (the content of rGO increases from 0.35 to 0.45 wt%) with content of rGO

rising, the maximum d_{33} value of 32.9 pC/N was obtained at 0.25 wt%. This result is well consistent with the variation law of output voltage and current in Fig. 4; Table 2.

3.3 Electrical characterization and properties of multi-layered composite film

In order to further enhance piezoelectric performance, multi-layered PVDF/BTO/rGO composite films with rGO addition content of 0.25 wt% were designed and systematical studied. Similarly, we prepared piezoelectric films with a total thickness of 60 µm and a number of 1 to 6 layers (single-layer thicknesses are equal) and packaged it into PNGs to test its corresponding output voltage and output current, as shown in Fig. 6. The output voltage and current increase first and then decrease, and the maximum value reaches (voltage of 16.91 V; current of 3.53 µA) at 4-layered structure design. It is found that the effect of the number of layered structure design on the output performance of PVDF/BTO and PVDF/BTO/rGO composite PNGs follows the same rules. While the composite film doped with rGO has higher output performance than the composite film

Fig. 6 Output performance of PVDF/BTO/rGO composite film with 1 to 6 layers, **a**, **b** open-circuit voltage; **c**, **d** short-circuit current
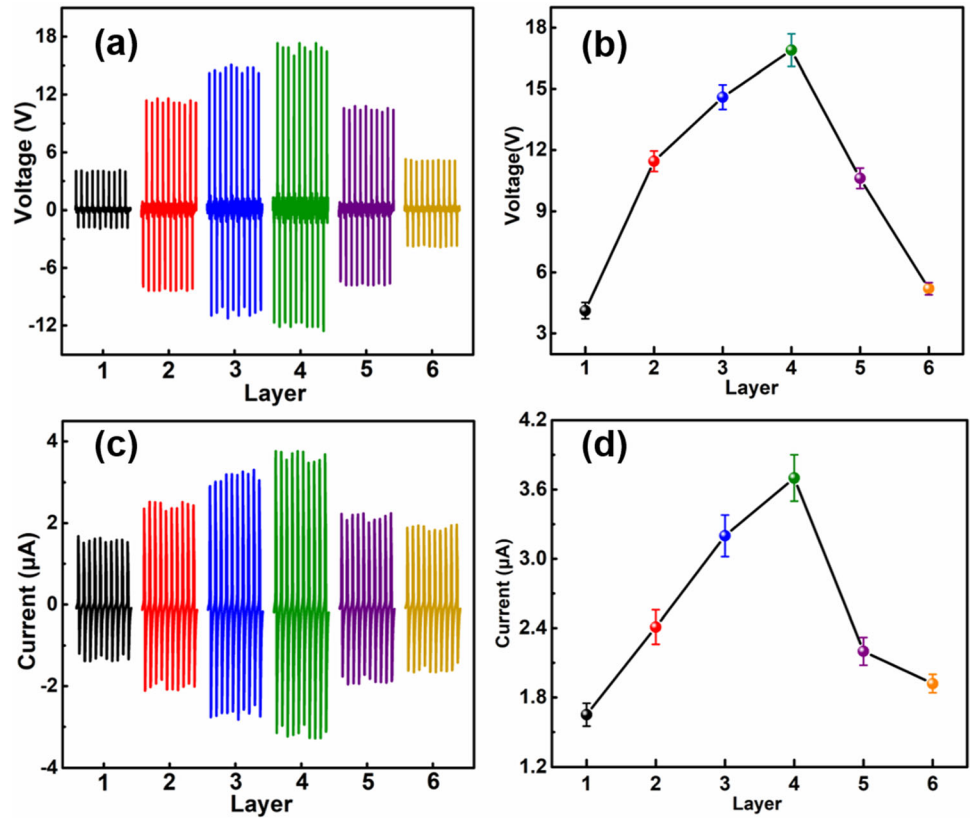
without rGO (the results are shown in Table S1), such as the output voltage and output current for 4-layered design with and without rGO composite PNGs are increased by 18.9% and 45.9%, respectively. It is mainly because rGO as a conductive phase significantly influences the piezoelectric performance of the composite film.

The output performance of PVDF/BTO/rGO piezoelectric composite film is the best under 4-layered structure design. Taken 4-layered structure design as an example, the relative permittivity and hysteresis loop of the 4-layered BTO/PVDF and BTO/PVDF/rGO piezoelectric composite film were measured. The influence of rGO on the dielectric and ferroelectric properties of piezoelectric composite films was explored. For convenience, we abbreviate the 4-layer BTO/PVDF piezoelectric composite film as BP_4, and the 4-layer BTO/PVDF/rGO piezoelectric composite film as BPR_4. Figure 7a shows the relative permittivity of BP_4 and BPR_4 in the frequency range of 1 kHz to 1 MHz at room temperature. It can be seen that the relative permittivity of BPR_4 is obviously higher than that of BP_4 as a whole, such as the

relative permittivity of BPR_4 is 46.19, and that of BP_4 is 26.75 at 1 kHz. This signifies that the introduction of rGO not only increases the interfacial polarization inside the composite material but also increases the dipole polarization. The hysteresis loop test was performed on BP_4 and BPR_4 at room temperature, and the result is shown in Fig. 7b. It can be seen that the remanent polarization of BPR_4 is higher than that of BP_4, the remanent polarization of BPR_4 is 1.16 $\mu C/cm^2$ higher than that value of BP_4 is 0.91 $\mu C/cm^2$. This may be because the introduction of rGO changed the domain microstructure of PVDF/BTO composites [25]. From the above results, it can be known that BPR_4-PNG based on the PVDF/BTO/rGO composite film exhibits excellent output performance; therefore, it becomes particularly important to explore the applicability of this PNG.

To test the feasibility of the practical application of PNGs, BPR_4 PNGs are connected with full-wave four-probe rectifier bridge and energy storage capacitor (10 μF, 22 μF). A schematic circuit diagram is displayed in Fig. 8a. The bridge rectifier is used to convert the AC signal generated by the composite

Fig. 7 The parameter measurement of BTO/PVDF composite with rGO and without rGO when the composite film is 4 layers: **a** Dielectric spectrum of BTO/PVDF composite with rGO and without rGO; **b** The polarization–electric filed hysteresis loops (P–E) of BTO/PVDF composite with rGO and without rGO
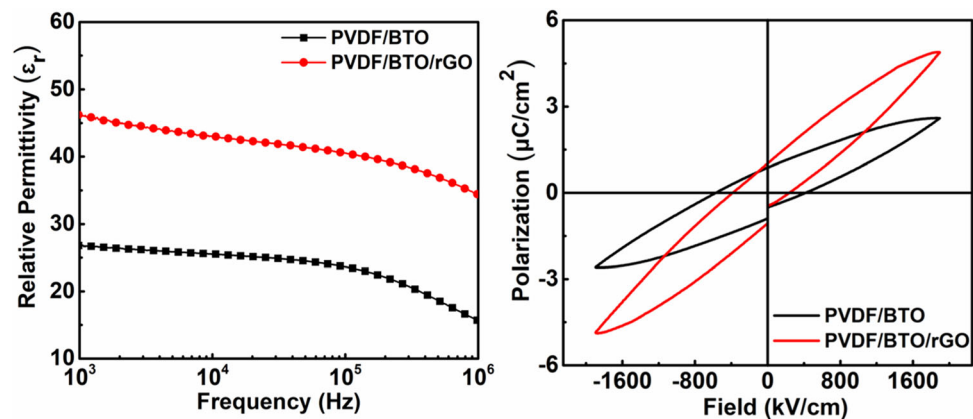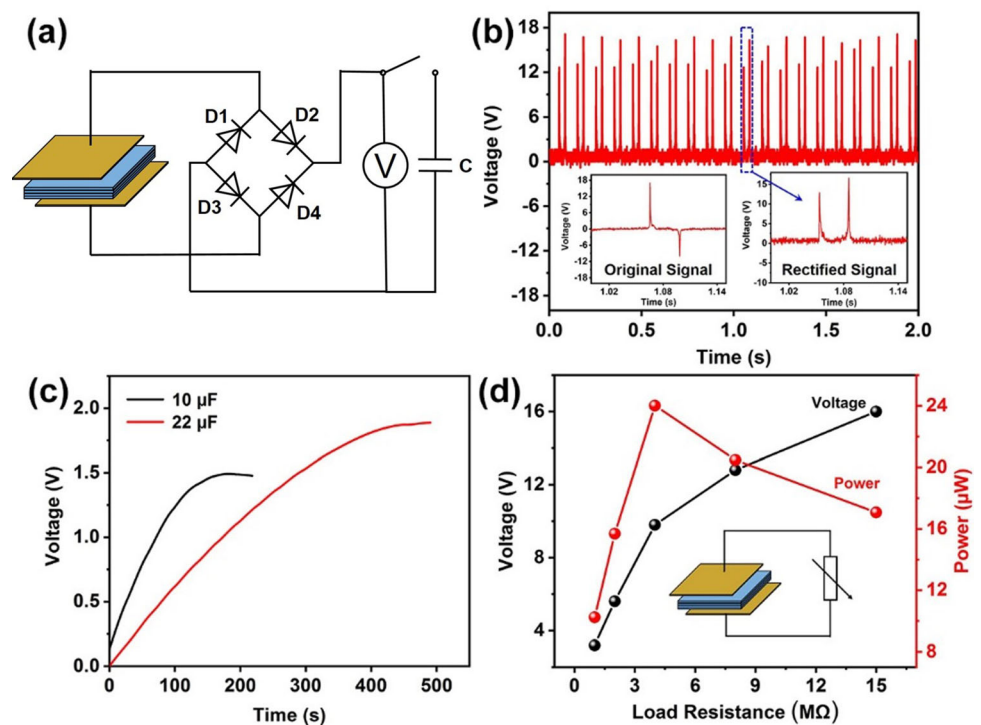

Fig. 8 **a** Schematic diagram of a piezoelectric nanogenerator charging capacitor; **b** Output voltage of a rectified piezoelectric nanogenerator; **c** Piezoelectric nanogenerator charging a capacitor (10 μF, 22 μF) process; **d** Output power test of piezoelectric nanogenerator

PNGs into DC signal, and then the output electrical signal is collected by an oscilloscope. The output signal after rectification is shown in Fig. 8b, and the images inset in is the signal before and after rectification. Two-capacity commercial capacitors (10 μF and 22 μF) were chosen to store rectified electric output generated by BPR$_4$ PNGs. 10 μF capacitor reaches a saturation value of 1.5 V after 120 s, while 22 μF capacitor reaches saturation value of about 2 V after 500 s. That suggests the composite PNGs take a short time to charge a capacitor with a relatively low saturation voltage, while acquiring a saturation value of a large capacitor is time consuming. The above experimental results show that flexible PNGs have

application prospects as power supply devices in some small electronic devices. To measure the maximum output power of PBR$_4$ PNGs, the output voltage against load resistance is shown in Fig. 8d. It can be clearly seen from Fig. 8d that the power of PBR$_4$ PNGs increases first and then decreases as the load resistance increases; when the load resistance is 4 MΩ, it reaches the maximum value of 24.01 μW. This value is 1.1 times higher than the power of BP$_4$ PNG without rGO doping in our previous work [25], which suggests doping with proper amount of conductive phase rGO could effectively improve the output performance of piezoelectric PNGs.

3.4 Application and stability test

Since our PBR$_4$ PNG is flexible and sensitive with fast response to various deformations and no considerable hysteresis, they have a strong potential for wearable device to detect the movements of the human body with large strains and high bending angles. In order to further demonstrate the capability of the flexible BPR$_4$ PNG for use on the human body, the PNG devices (3.5 cm × 3.5 cm × 5 mm) were pasted on an index finger knuckle, wrist, and elbow joint without any external power supply. The BPR$_4$ PNG is able to clearly distinguish joints bending different angles and the finger, wrist, and elbow bending are shown in Fig. 9a. With the enlargement of the bending angle, the tensile stress acting on the device enlarges, namely, the produced voltage signals are decided by motion bending angels. When BPR$_4$ PNG taped on finger joints was bent from 0° to 30°, 0° to 60°, and 0° to 90° at the frequency of 1 Hz, and the output voltages were 6.2, 10.1, and 17.3 V, respectively, which demonstrates that the output performance of BPB$_4$ is closely related with the deformations. The output voltage signals generated by wrist and elbow bending followed the similar rules. In addition, the output signals were clearly detectable in the repetitive bending/relaxing cycles without delay or drifting. To further demonstrate human body motion monitoring in real time, BPR$_4$ PNG was tape to the bottom of shoes and detect output signal under run, walk, and jump, as shown in Fig. 9b. From Fig. 9b, the order of the magnitude of the voltage signal is skip ∼ 18.2 V > run ∼ 8.1 V > walk 6.3 V, which is indicated that the self-powered flexible PNGs can monitor the body movement posture. On the basis of these experiments, the flexible BPR$_4$ PNGs used independently as a self-powered motion sensor for detecting the human joints and body movements without an external power demonstrated a strong capability to distinctively measure a wide range of human body motions and applicant in human health care and track activity.

The mechanical stability and reliability of PNGs are tested by continuous percussion experiments. As shown in Fig. 10, under a mechanical tap with a frequency of 10 Hz after 400 s, the amplitude of output voltage for 4-layered PBR$_4$ PNG did show a

Fig. 9 Monitoring of various human motions in real time. Output voltage as function of time for a typical PBR4 PNG **a** at different finger joint bending (30°, 60°, and 90°) motions; **b** at different wrist joint bending (30°, 60°, and 90°) motions; **c** at different elbow joint bending (30°, 60°, and 90°) motions **d** at walk, run, and skip deformations
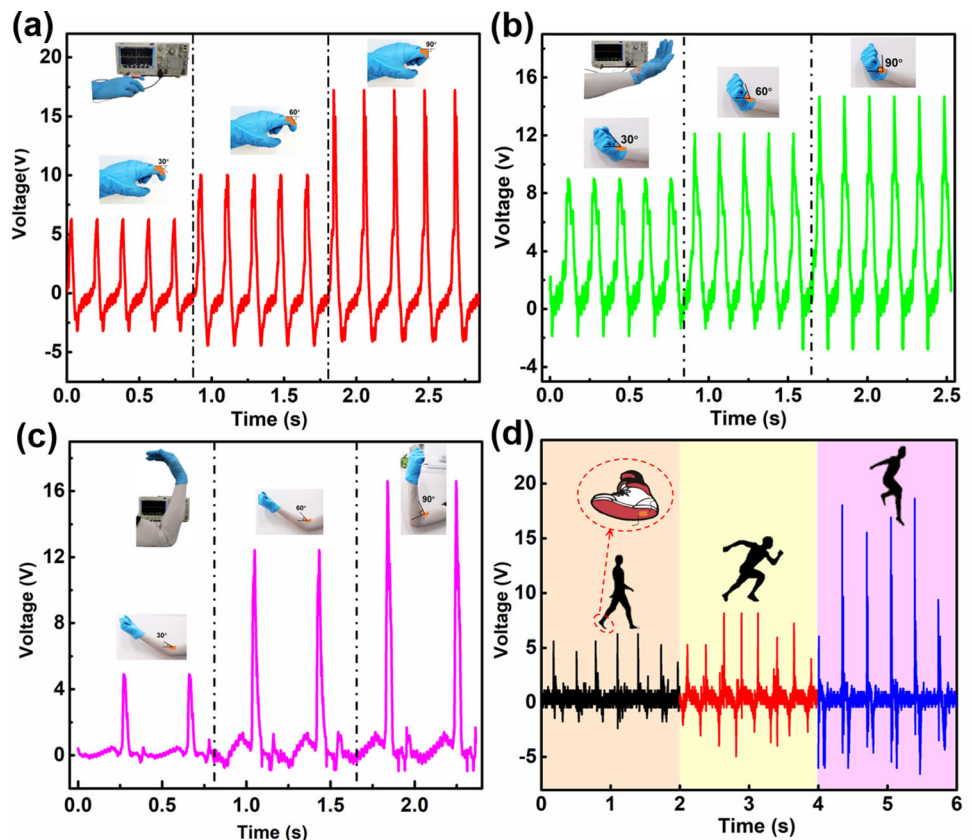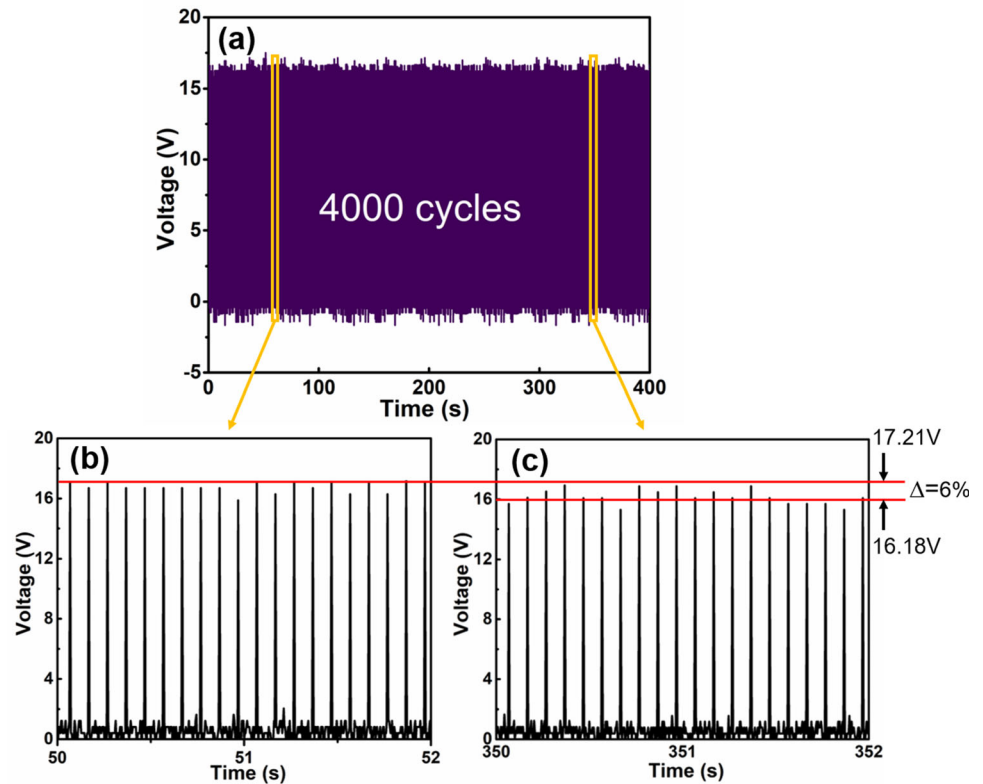
Fig. 10 Durability test of the BPR$_4$ PNG. **a** 4000 cycles; **b, c** shows partially enlarged views of (**a**)

small fluctuation 6% and remained constant, which proves that it is an effective and powerful energy. The applicability of the collector may be very suitable for energy harvesting applications driven by irregular excitation in our living environment.

4 Conclusions

This work demonstrates the successful synthesis of BTO/PVDF/rGO composite film with rGO content of 0, 0.15, 0.25, 0.35, and 0.45 wt% via a solution casting method. FTIR and Raman spectroscopy studies were conducted on the nanocomposite films displaying that the rGO propagates polar β-phase transition. The PNGs showed open-circuit voltage of 4.65 V and short-circuit current of 1.82 μA. A novel high-performance flexible multi-layered PVDF/BTO/rGO composite PNGs has been fabricated by layer-by-layer assembled method. The output voltage and current generated from the PBR$_4$ PNG with an rGO-doping content of 0.25 wt% can reach up to 16.91 V and 3.53 μA, which enhances 18.9% and 45.9% compared with PB$_4$ PNG without rGO, respectively. Relative permittivity and remanent polarization test

showed the piezoelectric properties and energy storage capability of the nanocomposite film, and PBR$_4$ PNG can charge capacitor within several minutes. A peak power density of 24.01 μW was shown by PBR$_4$ PNG when connected across a 4 MΩ resistor. This value is 1.1 times higher than the PB$_4$ PNGs. By periodic test over 4000 cycles of percussion and excitation via different deformations, durability and stability of the prepared multi-layered PBR$_4$ PNGs have been confirmed. Flexible PBR$_4$ PNGs were successfully applied to potential platforms for distinguishably detecting a wide range of human body joints movement and motion state in real time. Our approach for fabricating high-performance self-charged sensor is simple, low cost, and ergonomic; thus, it shows great promise for creating future flexible microelectronic devices in such application as wearable electronics, soft robotics, and artificial skins.

Author contributions

All authors contributed to the study conception and design. Material preparation, data collection, and analysis were performed by YL, JT, LK, YL, JS, HZ, CL, PL, JX, HJ, and KW. The first draft of the manuscript was written by YL, and all authors commented on previous versions of the manuscript. All authors read and approved the final manuscript.

Funding

Data availability

All data generated or analyzed during this study are included in this published article (and its supplementary information files).

Declarations

Conflict of interest The authors have no relevant financial or non-financial interests to disclose.

Ethical approval All procedures performed in studies involving human participants were in accordance with the ethical standards of the institutional and/or national research committee and with the 1964 Helsinki Declaration and its later amendments or comparable ethical standards.

Informed consent Informed content was obtained from all individual participants involved in the study.

Research involving human and/or animal participants This article does not contain any studies involving animals performed by any of the authors.

Supplementary Information: The online version contains supplementary material available at http s://doi.org/10.1007/s10854-021-07622-7.

References

1. J. Luo, L. Zhang, T. Wu, H. Song, C. Tang, Extreme Mech. Lett. **48**, 101279 (2021)
2. X.L. Qing, W.Z. Li, Y.S. Wang, H. Sun, Sensors **19**, 245 (2019)
3. Y. Yang, H. Pan, G.Z. Xie, Y.D. Jiang, C.X. Chen, Y.J. Su, Y. Wang, H.L. Tai, Sensor Actuat. A-Phys. **301**, 111789 (2020)
4. M.J. Xia, C.X. Luo, X.X. Su, Y.H. Li, P.W. Li, J. Hu, G. Li, H.B. Jiang, W.D. Zhang, J. Mater. Sci. Mater. Electron. **30**, 7558–7566 (2019)
5. W.J. Ding, W.W. Xu, Z.J. Dong, Y.Q. Liu, Q. Wang, T. Shiotani, Ceram. Int. **47**, 29681–29687 (2021)
6. N.T. Tien, T.Q. Trung, Y.G. Seoul, D.I. Kim, N.E. Lee, ACS Nano **5**, 7069–7076 (2011)
7. S.H. Shin, Y.H. Kim, M.H. Lee, J.Y. Jung, J. Nah, ACS Nano **8**, 2766–2773 (2014)
8. J.T. Li, J.J. Li, H.H. Wu, O.W. Zhou, J. Chen, T. Lookman, Y.J. Su, L.J. Qiao, Y. Bai, ACS Appl. Mater. Interfaces **13**, 38467–38476 (2021)
9. C.X. Luo, S.H. Hu, M.J. Xia, P.W. Li, J. Hu, G. Li, H.B. Jiang, W.D. Zhang, Energy Technol. **6**, 922–927 (2018)
10. X.M. Wang, F.Z. Sun, G.C. Yin, Y.T. Wang, B. Liu, M. D. Dong. Sensors **18**, 330 (2018)
11. E.J. Ko, S.J. Jeon, Y.W. Han, S.Y. Jeong, C.Y. Kang, T.H. Sung, K.W. Seong, D. K. Moon Nano Energy **58**, 11–22 (2019)
12. S.C. Chen, J.L. Luo, X.L. Wang, Q.Y. Li, L.C. Zhou, C. Liu, C. Feng. Sci. Rep. **10**, 8895 (2020)
13. S.K. Karan, D. Mandal, B.B. Khatua, Nanoscale **7**, 10655–10666 (2015)
14. W.H. Feng, J. Yuan, F. Gao, B. Weng, W.T. Hu, Y.H. Lei, X.Y. Huang, L. Yang, J. Shen, D.F. Xu, X.C. Zhang, P. Liu, S.Y. Zhang, Nano Energy **75**, 104990 (2020)
15. S.S. Duan, J. Wu, J. Xia, W. Lei. Sensors **20**, 2820 (2020)
16. X.M. Li, Z. Lv, H.W. Zhu, Adv. Mater. **27**, 6549–6574 (2015)

17. Z.F. Chen, X.M. Li, J.Q. Wang, L. Tao, M.Z. Long, S.J. Liang, L.K. Ang, C. Shu, H.K. Tsang, J. Xu, ACS Nano **11**, 430–437 (2017)

18. L. Li, X.M. Li, M.D. Du, Y.C. Guo, Y.C. Li, H.B. Li, Y. Yang, F.E. Alam, C.T. Lin, Y. Fang, Chem. Mater. **28**, 3360–3366 (2016)

19. X.M. Li, H.W. Zhu, K.L. Wang, A.Y. Cao, J.Q. Wei, C.Y. Li, Y. Jia, Z. Li, X. Li, D.H. Wu, Adv. Mater. **22**, 2743–2748 (2010)

20. X.M. Li, H.W. Zhu, Phys. Today **69**, 46–51 (2016)

21. U. Yaqoob, A.S.M.I. Uddin, G.S. Chung, RSC Adv. **6**, 30747–30754 (2016)

22. M.E. Achaby, F.Z. Arrakhiz, S. Vaudreuil, E.M. Essassi, A. Qaiss, Appl. Surf. Sci. **258**, 7668–7677 (2012)

23. R.K. Layek, A.K. Das, M.J. Park, N.H. Kim, J.H. Lee, Carbon **81**, 329–338 (2015)

24. L.H. He, G.M. Xia, J. Sun, Q.L. Zhao, R. Song, Z. Ma, J. Colloid Interface Sci. **393**, 97–103 (2013)

25. Y.H. Li, X.X. Su, K. Liang, C.X. Luo, P.W. Li, J. Hu, G. Li, H.B. Jiang, K.Y. Wang, Microelectron. Eng. **244-246**, 111557 (2021)

26. U. Yaqoob, A.S.M.I. Uddin, G.S. Chung, Appl. Surf. Sci. **405**, 420–426 (2017)

27. S. Badatya, A. Kumar, C. Sharma, A.K. Srivastava, J.P. Chaurasia, M.K. Gupta, Mater. Lett. **290**, 129493 (2021)

28. X.R. Hu, Z.T. Ding, L.X. Fei, Y. Xiang, Y. Lin, J. Mater. Sci. **54**, 6401–6409 (2019)

29. R. Bhunia, S. Gupta, B. Fatma, R.K. Prateek, A. Gupta, Garg, ACS Appl. Mater. Interfaces **11**, 38177–38189 (2019)

30. D.S. Gyan, A. Dwivedi, J. Appl. Phys. **125**, 024103 (2019)

31. M.Z. Ongun, S. Oguzlar, E.C. Doluel, U. Kartal, M. Yurddaskal, J. Mater. Sci. Mater. Electron. **31**, 1960–1968 (2020)

32. P. Martins, A.C. Lopes, S. Lanceros-Mendez, Prog. Polym. Sci. **39**, 683–706 (2014)

33. A. Anand, D. Meena, K.K. Dey, M. C. J. Polym. Res. **27**, 358 (2020)

34. M. Pusty, L. Sinha, P.M. Shirage, New J. Chem. **43**, 284 (2019)

35. Y.Y. Zhang, S.L. Jiang, Y. Yu, Y.K. Zeng, G.Z. Zhang, Q.F. Zhang, J.G. He, J. Appl. Polym. Sci. **125**, 314–319 (2012)

36. Y. Xia, R.Q. Gang, L. Xu, S.J. Huang, L.X. Zhou, J. Wang, Ceram. Int. **46**, 1487–1493 (2020)

37. S.K. Karan, D. Mandal, B.B.B. Khatua, Nanoscale **7**, 10655–10666 (2015)

38. X.L. Gou, Y.L. Bai, S.F. Zhao, J. Alloys Compd. **869**, 159313 (2021)

39. F. Guo, N. Jiang, B. Yang, S.F. Zhao, Appl. Phys. Lett. **114**, 253901 (2019)

40. Z.M. Dang, Y.H. Lin, C.W. Nan, Adv. Mater. **15**, 1625–1629 (2003)

41. L. Zhang, K.F. Chen, S. Wang, S. Chen, S.Y. Niu, Z.R. Wang, P.Y. Du, Mater. Lett. **233**, 306–309 (2018)

42. M.S. Khandekar, R.C. Kambale, J.Y. Patil, Y.D. Kolekar, S.S. Suryavanshi, J. Alloy. Compd. **509**, 1861–1865 (2011)

43. J.L. Zhang, P.F. Ji, Y.Q. Wu, X. Zhao, Y.Q. Tan, C.L. Wang, Appl. Phys. Lett. **104**(22), 222909 (2014)